JOURNAL OF MAGNETIC RESONANCE **134,** 287–299 (1998)
ARTICLE NO. MN981497

Localized Spectroscopy from Anatomically Matched Compartments: Improved Sensitivity and Localization for Cardiac ^{31}P MRS in Humans

Ralf Löffler,*,†,[1] Rolf Sauter,† Heinrich Kolem,† Axel Haase,* and Markus von Kienlin*,[2]

*Physikalisches Institut Universität Würzburg, Würzburg, Germany, and †Siemens Medizintechnik, Erlangen, Germany

Received August 25, 1997; revised April 23, 1998

Several pioneering studies have demonstrated that localized ^{31}P NMR spectroscopy of the human heart might become an important diagnostic tool in cardiology. The main limitation is due to the low sensitivity of these experiments, allowing only crude spatial resolution. We have implemented a three-dimensional version of SLOOP ("spectral localization with optimal pointspread function") on a clinical instrument. SLOOP takes advantage of all available *a priori* information to match the size and the shape of the sensitive volumes to the anatomical structures in the examined subject. Thus, SLOOP reduces the contamination from adjacent organs and improves the sensitivity compared to conventional techniques such as ISIS or chemical shift imaging (CSI). Initial studies were performed on six healthy volunteers at 1.5 T. The good localization properties are demonstrated by the absence of resonances from blood in the heart spectra, and by PCr-free spectra from the liver. Compared to conventional CSI, the signal-to-noise ratio of the SLOOP heart spectra was improved by approximately 30%. Taking into account the varying excitation angle in the inhomogeneous B_1 field of the surface coil, the SLOOP model computes the local spin saturation at every point in space. Therefore, no global saturation correction is required in the quantitative evaluation of local spectra. In this study, we found a PCr/γ-ATP ratio in the left ventricular wall of 1.90 ± 0.33 (mean ± standard deviation). © 1998 Academic Press

Key Words: **cardiac spectroscopy; high energy phosphates; quantification; spatial response function; SLOOP.**

INTRODUCTION

Localized phosphorus NMR spectroscopy of the human heart provides a noninvasive method to measure high energy metabolites. The potential of *in vivo* ^{31}P spectroscopy for cardiac diagnosis was recognized early (*1*). Several clinical studies have demonstrated alterations of adenosine triphosphate (ATP), phosphocreatine (PCr), and inorganic phosphate (P_i) under pathologic conditions. Weiss *et al.* (*2*) showed a significant decrease of the PCr/ATP ratio during exercise in patients with coronary artery disease. In patients with dilated cardiomyopathy, Neubauer *et al.* detected a decreased PCr/ATP ratio, which correlated with NYHA classification, and improved after drug therapy (*3*). Recently, Yabe *et al.* (*4*) demonstrated that determination of the absolute concentration of ATP in myocardial tissue may be a clinically important method to evaluate myocardial viability in coronary artery disease. The current status of cardiac ^{31}P spectroscopy has been reviewed recently (*5–7*).

Several techniques have been used to acquire cardiac spectra in human subjects: Rotating-frame MRI (*8*), DRESS (*1*), and ISIS (*9*) were early methods for cardiac spectroscopy. Chemical shift imaging (CSI) (*10*) is used to a growing extent in cardiac spectroscopy: One-dimensional (1D) CSI is used together with other methods for spatial localization in the two remaining dimensions (*11, 12*). 3D-CSI (*13–16*) with phase encoding in three spatial dimensions, or 2D-CSI with slice selection (*17, 15*) (also termed 3D spectroscopic imaging) need no further localization. 3D-CSI has the advantage that the voxel can be shifted in every spatial dimension after the experiment has been carried out. However, it also requires a higher minimal number of phase encoding steps.

All these methods have to find a compromise between sensitivity and spatial localization. (3D-CSI, for example, is able to detect only a part of the available magnetization (*18*) because of phase encoding. A similar reasoning applies to slice profiles.) At the same time, the spatial resolution is low because of the low phosphorus signal. Although sensitivity has been improved with phased array coils, ^{1}H decoupling, and nuclear Overhauser effect (NOE), spatial resolution is still the limiting factor in experiments (*5*).

The volumes which can be addressed by the foregoing methods are in most cases cuboidal, whereas the anatomical features of interest are curved and approximately in the same size as the voxel. This leads to voxel bleed and partial volume effects (*19*).

If absolute quantification of metabolites is desired, calibration factors have to be introduced, which requires endo- or exogenous concentration references. The effect of an inhomogeneous coil excitation and reception, as is normally found with cardiac spectroscopy, has to be taken into account. The

[1] Current address: Abteilung für Radiologische Diagnostik, Klinikum Großhadern, Universität München, München, Germany.

[2] To whom correspondence should be addressed: Markus von Kienlin, PD Ph.D, Physikalisches Universität Würzburg, Am Hubland, 97074 Würzburg, Germany. Fax: +49 931 706297, E-mail: kienlin@physik.uni-wuerzburg.de.

1090-7807/98 $25.00

voxel is only partly filled with the tissue to be quantified. The different relaxation times of the metabolites have to be considered if the repetition time is in the order of the relaxation time or shorter when exciting with large flip angles (*4, 20*).

The aims of our studies were to improve sensitivity and spatial resolution of the spectra. This can be achieved by matching the regions of interest (ROI) with the anatomical structures to be investigated; this *a priori* information is gained by MR imaging. With the application of all known experimental parameters to the model (B_1 field distribution, relaxation times of the metabolites, repetition time of the experiment), one is able to quantify the metabolic content in the different ROIs.

We applied the SLOOP (spectral localization with optimal pointspread function) technique first described by von Kienlin and Mejia (*21*). In extension to the original work, we used a 3D acquisition scheme. The SLOOP algorithm was altered to consider all available experimental parameters.

THEORY

Reconstruction Algorithm

According to the principles of reciprocity (*22*) and spin saturation (*23*), the initial amplitude and phase of the NMR signal emanating from a given point $\vec{r}$ in space which is detected in a pulse-acquire phase encoded NMR experiment is given by

$$s_m(\vec{r}) = B_1(\vec{r}) \cdot A \cdot \frac{\sin \alpha(\vec{r})(1 - \exp(-T_r/T_1(\vec{r})))}{1 - \cos \alpha(\vec{r})\exp(-T_r/T_1(\vec{r}))} \times \exp(-i \cdot \vec{k}_m \cdot \vec{r}) \cdot \rho(\vec{r}). \quad [1]$$

The first part of the right-hand side of Eq. [1] describes the dependency of the received signal on the transmitter coil: $B_1(\vec{r})$ is the radiofrequency (RF) field profile of the receiver coil. The proportionality coefficient A only depends on the hardware of the instrument and will be set to $A = 1$ from now on. The middle part is determined by the receiver coil sensitivity and the repetition time: $\alpha(\vec{r})$ is the local excitation flip angle. For a single transmit/receive coil the flip angle $\alpha(\vec{r})$ is proportional to $B_1(\vec{r})$. T_r is the repetition time of the experiment. $T_1(\vec{r})$ is the longitudinal relaxation time. The T_1 value of each resonance can be organ specific and is therefore spatially dependent. The phase factor $\exp(-i \cdot \vec{k}_m \cdot \vec{r})$ is the effect of phase encoding, m is the running index of the phase encoding, and $\rho(\vec{r})$ denotes the spin density.

The vector $\vec{k}_m$ is determined by

$$\vec{k}_m = \frac{\gamma}{2\pi} \int \vec{G}_m(t)dt, \quad [2]$$

where γ is the magnetogyric ratio and $\vec{G}_m(t)$ the strength of the mth phase encoding gradient.

At every phase encoding step, signal from the whole sample is detected:

$$p_m = \int_V s_m(\vec{r})d\vec{r}. \quad [3]$$

Let us assume for the time being that the examined object consists of N compartments of respective volumes V_n with according homogeneous spin densities $c_n := \rho(\vec{x})|_{\vec{x} \in V_n}$. In this case, Eq. [3] can be written as

$$p_m = \sum_n \int_{V_n} s_{mn}(\vec{r})d\vec{r}, \quad [4]$$

where the index n denotes the regional compartments. Integration is over the volume V_n of the respective compartment n.

To find a solution for the spin densities c_n in the N compartments, one can utilize the SLOOP algorithm (*21*), which is based on SLIM (spectral localization by imaging) introduced by Hu *et al.* (*24*). Equations [1] and [4] can be combined:

$$p_m = \sum_n g_{mn}c_n, \quad [5]$$

with g_{mn}:

$$g_{mn} = \int_{V_n} B_1(\vec{r}) \frac{\sin \alpha(\vec{r})(1 - \exp(-T_r/T_{1n}))}{1 - \cos \alpha(\vec{r})\exp(-T_r/T_{1n})} \times \exp(-i\vec{k}_m \cdot \vec{r})d\vec{r}) = \int_{V_n} a_n(\vec{r})\exp(-i\vec{k}_m \cdot \vec{r})d\vec{r}. \quad [6]$$

The factor $a_n(\vec{r})$ contains all parameters which are not influenced by the phase encoding (T_1 saturation, transmit/receive characteristic of the coil). The most important property of the coefficients g_{mn} is their independence of the actual experiment, i.e., only the *a priori* information contributes to g_{mn}. The accuracy of the calculation of the coefficients is therefore not deteriorated by the noise level of the experiment.

All phase encoding steps combined in a system of linear equations can be expressed in matrix form,

$$\vec{P} = \mathbf{G}\vec{C}, \quad [7]$$

and can be solved for $\vec{C}$ by singular value decomposition (SVD):

$$\vec{C} = \mathbf{H}\vec{P} \quad \text{with} \quad \mathbf{HG} = \mathbf{1}. \qquad [8]$$

H is the pseudo inverse matrix of **G; 1** is the identity matrix.

With this method, it is possible to access the concentration of the NMR visible metabolites in the individual compartments. From Eq. [8] it can be concluded that the compartmental signals c_n are gained by a linear combination of the measured signals p_n with weighting functions h_{nm}, similar to the Fourier transform. Further postprocessing of the signals c_n can be performed in analogy to conventional spectroscopy. Since all resonances in a spectrum generally have different T_1 values, the calculation of the matrix **G** has to be repeated with the according T_{1n} for every resonance to be examined. This leads to a set of spectra for each resonance. The quantitative evaluation of a resonance has to be performed on the spectrum which was calculated with the appropriate T_1 value. No further saturation correction is needed, since the T_1 relaxation is already considered in the model (Eq. [6]).

Spatial Response Function

The best way to understand the localization mechanism and the properties of SLOOP is to analyze its spatial response function (SRF) (*25, 26*). Indeed, the analysis and the optimization of the SRF are the key elements in SLOOP localization. The SRF indicates how every point in the sample contributes (in amplitude and phase) to a localized spectrum. A localized spectrum obtained in any phase-encoded experiment thus results from the actual spin distribution, which is weighted by the SRF and then integrated over the sample. The SRF of a conventional, unfiltered CSI experiment is a Bessel function with its characteristic sinc shape (*27*). Localization in CSI arises from the high amplitude of the SRF within the ROI. Nevertheless, the nonzero amplitude of the SRF outside the ROI may be the origin of substantial spatial signal leakage in CSI (*28, 29*).

For SLOOP, it is not possible to indicate a general shape of the SRF as can be done for CSI. In every new experiment, the SRF needs to be calculated for each compartment. Taking inhomogeneous transmit and receive coils as well as spatially varying spin saturation into account, the SRF corresponding to the SLOOP spectrum of compartment n is given by (*21*)

$$\mathrm{SRF}_n(\vec{r}) = \sum_m h_{nm} \cdot a_n(\vec{r}) \cdot \exp(-i\vec{k}_m \cdot \vec{r}). \qquad [9]$$

Note that this formula is a concatenation of Eqs. [6] and [8], with the exception that it evaluates a single point in space instead of the integral over the whole sample. As can be seen from Eq. [9], the SRF depends on the parameters of the measurement protocol (i.e., the phase encoding gradients, the B_1 field distribution, and the reconstruction coefficients), but not on the actual spin distribution in the sample or the signal-to-noise ratio in the measured data. Just as a rectangular function can be approximated by a linear combination of appropriately weighted, harmonic functions in Fourier series analysis, the SRF is the result of the spatially varying phase patterns induced by the phase encoding gradients, which are recombined with the reconstruction coefficients h_{nm}.

The particular reconstruction algorithm used in SLIM and SLOOP leads to an interesting property of their SRFs. The SVD computation of the pseudo inverse **H** of **G** implies that $\mathbf{H} \cdot \mathbf{G} = \mathbf{1}$ (see Eq. [8]). From this condition, one can derive that the integral of the SRF over the compartment of interest yields exactly 1 (the diagonal elements of the identity matrix), while the integral of the same SRF over all other compartments yields zero (the off-diagonal elements). This result does not depend on the experimental parameters; it is especially true for virtually any set of values for the phase encoding gradients. (In rare and rather academic situations, the system may degenerate, and there might be no mathematical solution to the pseudo inverse of **G.** In this case one or more singular values of **G** are zero.)

This particular property of the SRF is the very basis of the localization mechanism in SLIM: the contribution to the signal from the ROI from all other compartments is nulled because of phase cancellation. This phase cancellation, however, may fail if the initial condition about homogeneous compartments is not satisfied. Any heterogeneity in the compartments—e.g., nonuniform spin distribution, susceptibility-induced shifts of the static magnetic field—may lead to substantial spatial leakage (*30*).

To obtain a reliable localization where heterogeneity in the compartments does not lead to spatial contamination, the SRF has to meet additional requirements. It should have high and uniform amplitude and phase within the ROI, and a very low amplitude anywhere else. SLOOP fulfills this condition as far as possible, trying to match the SRF to the size and the shape of the anatomical compartments by choosing optimal experimental parameters, in particular, appropriate phase encoding gradients. As in CSI, localization is then mainly based on the amplitude distribution of the SRF, and phase cancellation is only an additional mechanism which further improves localization. A quantitative measurement of the quality of the SRF is the localization criterion $\mathcal{L}$, which is defined as (*21*)

$$\mathcal{L}_n = \int_{\text{Volume}\neq\text{ROI}} \left|\mathrm{SRF}_n(\vec{r})\right| d\vec{r}. \qquad [10]$$

The smaller $\mathcal{L}_n$, the lower the amplitude of the SRF outside the ROI, and the better the quality of localization. The integral over the SRF within the ROI is *per definitionem* equal to 1; therefore, this criterion indicates the worst-case contamination relative to the actual signal amplitude. This quantitative criterion to evaluate the quality of localization allows the choice of those experimental parameters which yield the best SRF for the regions of interest. $\mathcal{L}$ is a much stricter criterion than the

comparable "contamination" defined by the EEC COMAC-BME Concerted Action (*31*). In the latter, "contamination" is determined experimentally in a defined phantom setup, while the localization $\mathcal{L}$ is a theoretical criterion indicating the probability of contamination in the worst possible case.

The preceding definition of a localization criterion, which is based on the absolute amplitude of the SRF, has been chosen because it relates directly to the strength of leaking signals. Other definitions are possible, and a criterion based on the energy of the SRF outside the ROI might be of particular interest. Such a criterion might be more appropriate to evaluate the presence of local "hot spots" in the SRF. The localization criterion just given inherently includes the "limited support assumption" (*32*), which exploits the fact that any signal can only originate from locations within the sample.

The overall performance of any method for localized MRS depends not only on its quality of localization, but also on its sensitivity. Indeed, the experimental duration of most MRS examinations is governed by the low signal-to-noise ratio, and any method should be as efficient as possible in exploiting the available spin magnetization. In general, improving the spatial resolution is detrimental to the sensitivity, and the best compromise between both requirements has to be sought in any application. In every localized MRS experiment some signal is inevitably lost because of intravoxel phase dispersion and/or slice selection, saturation effects, inhomogeneous B_1 fields, etc. The signal loss relative to a hypothetical no-loss experiment, where all outside contributions are eliminated without affecting the magnetization of the target volume, with infinitesimal long repetition time, perfect excitation, and optimal sensitive reception can be determined. For SLOOP this fraction of detected versus available magnetization in each compartment is given by the "efficiency" $\mathcal{E}$ (*21*):

$$\mathcal{E}_n = \frac{1}{V_n \sqrt{\sum_m |h_{nm}|^2}}. \qquad [11]$$

Comparing different localization techniques with this criterion can be difficult, since it also contains parameters which cannot be influenced by the NMR method (T1, coil sensitivity). In order to quantify only the influence of the phase dispersion, other dependencies should be eliminated. We therefore define the "SLOOP efficiency" $\mathcal{E}_{n\mathrm{SLOOP}}$ as

$$\mathcal{E}_{n\mathrm{SLOOP}} = \frac{\mathcal{E}_n V_n}{a_n}, \qquad [12]$$

where a_n is defined in Eq. [6].

$\mathcal{E}_{n\mathrm{SLOOP}}$ allows the direct comparison of SLOOP with other phase encoding techniques, since only the signal loss due to phase dispersion is considered. $\mathcal{E}_n$ would be equal to 100% in the ideal case that no signal is lost. For unfiltered CSI, the signal loss due to phase dispersion amounts to 13% per spatial dimension (*18*), and consequently the SLOOP efficiency $\mathcal{E}_{n\mathrm{SLOOP}}$ of a 3D CSI voxel is only 67%. This criterion is similar to the "selection efficiency" defined by the EEC Concerted Action (*31*). The difference is that the SLOOP efficiency is a theoretical criterion applicable to any selected volume, whereas the selection efficiency is determined experimentally in a defined phantom.

With these two criteria to evaluate the quality of the SRF and the sensitivity, one can modify the parameters of a SLOOP experiment for a given setup until the best solution has been found. So far, we know of no analytical procedure which could provide directly the best set of experimental parameters. We therefore used a numerical optimization scheme where a computer evaluates the properties of a SLOOP experiment in a given setup, and modifies the variable parameters of the experiment (namely, field of view (FOV), α, number of accumulations) until the best combination of localization and sensitivity is found. Figure 1 shows a flow chart on how the SLOOP reconstruction and SLOOP optimization is performed.

SLOOP reaches its full potential when applied in all three spatial dimensions. The match of the SRF to the shape of the anatomical compartment ensures that most of the magnetization (as indicated by the efficiency $\mathcal{E}$) within this compartment contributes to the signal detected. This is true even if the ROI has a concave shape. In CSI, the size of the voxels either has to be chosen small enough to avoid contamination from adjacent tissue, which implies loss of sensitivity due to the smaller voxel volume, or the voxels have to be made large to get a high SNR, which results in a contamination from adjacent tissue. With SLOOP, the acquired signal can be maximized and the contamination minimized simultaneously.

METHODS

Measurement Protocol

In implementing the method, it was our primary goal to ensure that the method can be used in a normal clinical setting. Therefore, we first performed phantom measurements to validate our method and to prove the quantification capabilities of the algorithm. Then we conducted *in vivo* experiments in six volunteers to test the protocol and to compare the technique with conventional methods. We implemented SLOOP on several scanners (MAGNETOM SP and MAGNETOM VISION, Siemens Medizintechnik, Erlangen) with broadband capabilities. The field strength of these scanners was 1.5 T. For the SP systems, we also used a second RF transmit channel to permit the utilization of proton decoupling and nuclear Overhauser enhancement (NOE). The VISION systems were used in standard configuration, allowing only the use of NOE.

The measurement protocol utilized resembled the measurement protocol which has been used in the past for measuring 3D CSI phosphorus spectra in the human heart (*15*). The coil used was a custom-made double resonance coil consisting of

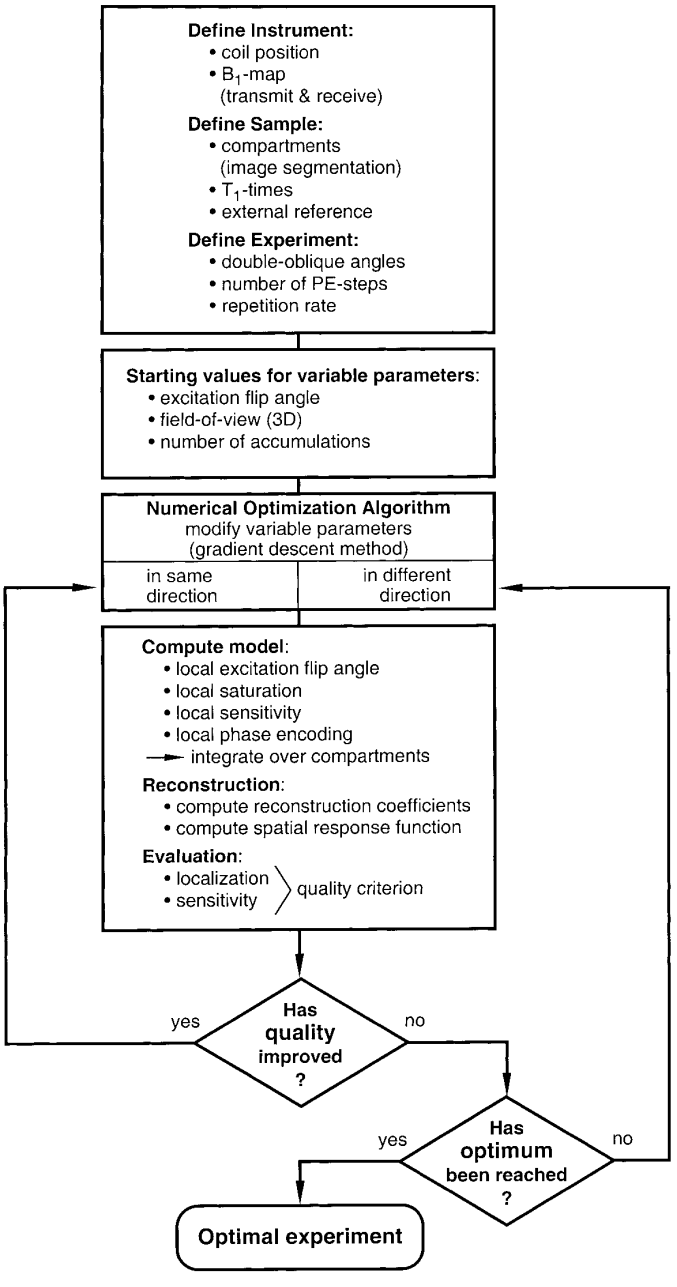

FIG. 1. Flow chart of the SLOOP optimization and reconstruction: If an optimization is performed, the decision path is iterated according to the actual condition. If a SLOOP reconstruction is carried out, the main branch is executed once. This supplies the quality criteria and the reconstruction coefficients used to calculate the SLOOP spectra from the measured FIDs.

two concentric loops. The outer loop is a ^{1}H transmit/receive loop of 17 cm diameter and the inner loop is a ^{31}P transmit/receive loop of 11 cm diameter. The proton coil was arranged about 1 cm farther from the patient to avoid the risk of hot spots in decoupling and to get a more homogeneous RF profile over the region of interest. Together with coil housing and support for the patient, this resulted in a total coil distance of about 3 cm from the patient's skin.

The first step in the protocol was the acquisition of scout images to determine the position of the coil and of a reference vial. The coil position and orientation has to be known to allow the transformation of the standard B_1 field characteristic of the coil to the actual spatial coordinates of the experiment. Therefore, we fixed five silicone-filled capillaries arranged in a square with a diagonal below the coil. Thus, it was possible to determine the exact coil position with just two parallel images on which three capillaries were visible. The chemical shift of the silicone was corrected before the images were analyzed. After this, high resolution proton images were acquired for 3D segmentation. The imaging sequences differed for phantom and volunteer examinations (see later discussion).

After imaging, we shimmed to get a water linewidth better than approximately 15 Hz full width half maximum (FWHM) in the phantom and 30 Hz FWHM in volunteers. The flip angle generated at one point in space by a pulse with a known power integral had to be determined to get a calibration point for $\alpha(\vec{r})$. Therefore, we attached a small vial in proximity to the coil filled with 1.3 ml methanol saturated with phenylphosphonic acid, which has resonances well away from any physiologically relevant resonances. Calibration was done by successively increasing the voltage of the RF pulse in an FID sequence to determine the 180° pulse at the position of the vial.

The spectroscopic data were acquired with a 3D CSI sequence with a nominal FOV for the CSI matrix of $200^2 \times 400$ mm^3. The matrix size was 8^3. We sampled 512 data points in 256 ms resulting in a bandwidth of 2 kHz. No volume preselection was used. The 3D CSI matrix could be rotated freely in space. The long axis of the voxel was aligned to the long axis of the heart in a double oblique manner (*15*). T_r was one RR interval, ranging from 0.8 to 1.1 s in the examined volunteers. The excitation pulse was a rectangular pulse with a duration of 320 μs; the center frequency of the RF pulse was in the middle of the PCr and γ-ATP resonances. The acquisition delay after the RF pulse needed for phase encoding was 900 μs. To achieve a better signal-to-noise ratio, we utilized the nuclear Overhauser effect by applying three nonselective ^{1}H saturation pulses prior to each ^{31}P scan. The NOE enhancement was rather uniform over the volume of interest (VOI) since the proton coil was large compared to the phosphorus coil. The time constant for the NOE to build up and to vanish is on the order of several seconds. The application of three nonselective NOE pulses with a duration of 2 ms and a pulse amplitude of 80 V in an RR interval was therefore strong enough to drive the magnetization in an equilibrium state over the whole VOI while complying with SAR regulations (*33*).

Postprocessing was performed on a stand-alone workstation (Sun Sparc™ 10) with software modules written in IDL (Interactive Data Language). One step of the postprocessing was the segmentation of the proton images. In our setup, the rather small proton coil led to large B_1 field variations over the FOV, which are difficult to handle by automated segmentation algo-

rithms. The segmentation was therefore performed manually, slice by slice, with a variety of supporting tools (*34–37*).

After segmentation, the SLOOP algorithm was used for the acquired data. Spectra were reconstructed using the respective T_1 values of PCr and γ-ATP as input variables. The reconstruction was repeated for every resonance with the appropriate T_1 value. To allow the evaluation of the SLOOP parameters, $\mathscr{E}$ and $\mathscr{L}$ for all compartments, together with other characteristic information such as compartment volume and measured SNR, were also issued by the SLOOP software. The flow chart of Fig. 1 shows the steps of the SLOOP reconstruction.

Further postprocessing of the calculated FIDs was done with the standard spectroscopy postprocessing software available on the VISION scanner. The FIDs were zero-filled and a line broadening of 4 Hz was applied. After Fourier transform, all spectra received the same zero- and first-order phase correction.

Metabolite ratios were determined by the integrals of fitted Gaussian peaks. Fitting was done on the phase-corrected real part spectra with the restricted line fit algorithm of the postprocessing software. No baseline correction was done.

The raw data were also postprocessed to get CSI spectra. The grid was shifted along the short axis to cover the anterior wall with two voxels and in the direction of the long axis so that no chest muscle was included within the nominal voxel boundaries. No spatial filter was applied. Further spectral treatment was exactly as for the SLOOP spectra to allow comparison with SLOOP.

Phantom Measurements

The SLOOP method depends on good agreement between model and actual experiment. Phantom measurements were performed to validate the model and the implementation of the algorithm.

In a first step, the phases of the signal generated by a point source at different phase encoding steps were compared to the phase shift calculated by the software with the given experimental parameters. When the calculated and the measured phase shift are identical, factors which cause a phase shift in Eq. [6], namely, the spatial coordinates $\vec{r}$ and $\vec{k}$, are treated correctly. This allows, for example, the identification of errors due to misregistration in the proton images or eddy currents during spectroscopy acquisition. Errors would manifest in a different slope of the two lines, which can be easily identified.

The phantom used for these experiments was a small vial filled with 1 ml 1.0 M H_3PO_4 buffer solution. In subsequent measurements, it was positioned at different points in space. Proton images were acquired to allow the spatial registration of coil and phantom, and a phosphorus 3D CSI experiment was conducted. Because of the orthogonality of the gradients, it is sufficient to extract and treat only the central lines from the CSI data set (i.e., $k(x, 0, 0)$, $k(0, y, 0)$, and $k(0, 0, z)$). The phases of these experimental signals were compared to the calculated results.

To validate the localization properties and correct quantification, experiments were performed with a phantom consisting of several compartments. Four bottles of different volumes, containing different concentrations of H_3PO_4 solution, were submerged into a larger flask containing physiological saline solution without any phosphate. We determined the T_1 time of the phosphate with an inversion recovery sequence to be 650 ms. Acquisition of the spectroscopic data was done in coronal direction.

Volunteer Measurements

We performed measurements on 6 healthy volunteers (5 male and 1 female, age 20–32 years), who gave their informed consent. The volunteers were positioned prone on the coil system to reduce breathing artifacts and to restrict motion of the heart. In this position, the heart comes closer to the chest wall, and thus to the coil system, leading to better SNR.

The high resolution image data set used for segmentation were cardiac triggered, segmented 2D-FLASH short axis images. The matrix size was 256×144 with a FOV of $(300\ \text{mm})^2$ and a slice thickness of 8 mm. We acquired 20–22 slices with no slice gap, depending on the subject's anatomy. The acquisition time for these images was 10–20 min, depending on heart rate. The 3D CSI matrix was oriented parallel to the short axis images. Four averages per phase encoding step were sampled. Acquisition was triggered to every heartbeat; sampling started 200 ms after the R wave, in the late systole. The whole experiment, including setup, imaging, and spectroscopy, took less than 1 h.

The 3D-image stack covering the VOI of the CSI acquisition was used for subsequent segmentation of the anatomical compartments. Usually the following compartments were segmented in volunteers: The LV-wall compartment consisted of the left myocardium, including septum and excluding the papillary muscles. The LV compartment was the left ventricle with the papillary muscle. The RV compartment was made of the right ventricle and the right ventricular wall (since it was too thin to be segmented separately). The chest wall compartment included the whole chest wall with ribs. Left and right atrium and the large vessels from the heart as far as visible were also segmented into one compartment. If visible, the aorta descendens was segmented. The remaining signal void in the thorax was attributed to the lung. The last anatomical compartment was made of the liver. The reference vial was also segmented. The T_1 values used for reconstruction of the compartments from the heart (see Eq. [6]) were the averages of values collected by Bottomley (*5*) from various sources, specifically $T_{1(\gamma\text{-ATP})} = 2.4$ s and $T_{1(\text{PCr})} = 4.4$ s. The T_1 values used for the liver compartment were $T_{1(\text{ATP})} = 0.42$ s and $T_{1(\text{PCr})} = 4.4$ s, and for the chest wall compartment, $T_{1(\text{ATP})} = 4.3$ s and $T_{1(\text{PCr})} = 6.5$ s (*38*). For the lung compartment, the same values as for the heart compartments were used.

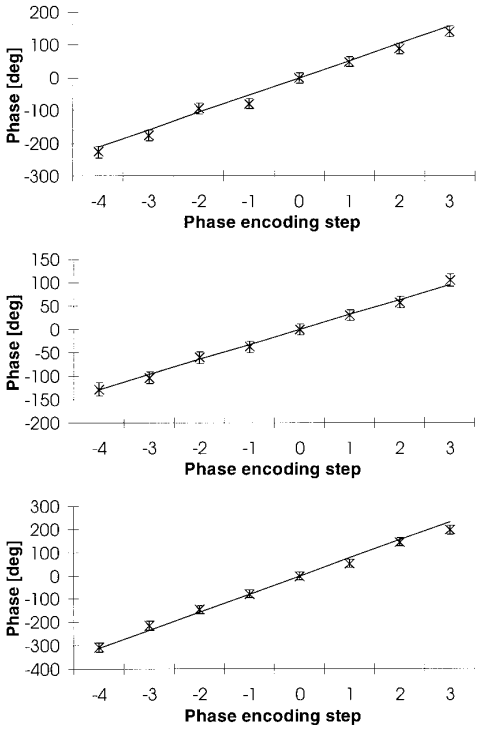

FIG. 2. Theoretical and measured phases of the MR signal detected after different phase encoding steps from a small, off-center sample. Within the SNR limit, there is excellent agreement between the values predicted from the theoretical model (straight lines) and the measured values (crosses) for all three gradient directions (x: top, y: middle, z: bottom). The phase errors of the calculated data points were determined from the SNR of the respective phase encoding step (*39*).

RESULTS

Phantoms

To prove the concordance of model and reality, the measurements with the point sample were repeated with different positions of the small vial and with different orientations of the CSI matrix. An example of the results is given in Fig. 2. The straight lines indicate the phase changes calculated from the model; crosses indicate the phase differences measured. In this particular experiment, the sample was positioned off-center to a different degree for each spatial dimension. In a large number of measurements, we always obtained good agreement between expected and calculated phase shifts. The difference between measured and calculated data points in the measurement of Fig. 2 is only due to the low SNR (each data point represents just one phase encoding step!), as indicated by the error bars. Errors of the model would manifest in a deviation from the calculated slope.

Table 1 summarizes the results of a measurement with the four-bottle phantom shown in Fig. 3, indicating the real volumes of the bottles and the calculated volumes obtained from the segmentation procedure. The volume of the container is not shown, since it was partly outside the sensitive volume of the coil. The parameters from the SLOOP reconstruction are also depicted. Figure 3 displays the spatial response function of the compartments of the phantom in one coronal slice. The SLOOP spectra from the five compartments are also depicted in Fig. 4.

The quality of the localization can be verified with the spectrum of the container. This signal is 100-fold smaller than the others and dispersive. Thus, the signal can be interpreted as an uncanceled contribution from an outside region, which may originate from an imperfect shim, rather than stemming from within the compartment, which contained no phosphate. The differences in the linewidths of the other spectra are due to varying shim conditions.

The peak areas of the different compartments are also given in Table 1. In Fig. 4, the peak area is plotted as a function of the real phosphate concentration, displayed as crosses. The solid line is the line fitted to the values by a single parameter fit (slope). The regression coefficient of the fitted line is $r = 0.995$. This demonstrates that although the compartments have different volumes, are subjected to different B_1 fields, and even the resulting spectra have different linewidths, it is still possible to determine the phosphate concentration very accurately.

Volunteers

Figure 5 shows one out of 21 double oblique proton images in a volunteer. Overlaid on the proton image are the borders of the segmented compartments. The segmentation information from all slices is used to get the compartmental volumes used for reconstruction.

The segmentation also yields the volumetric values. The

TABLE 1
SLOOP Parameters in the Phantom Measurement

Compartment	True volume (ml)	Measured volume (ml)	Localization $\mathcal{L}$	Efficiency (%) $\mathcal{E}_{SLOOP}$	Fitted peak areas (a.u.)
Container			0.042	15	0.0
Bottle 1	48	46	1.4	62	1.86
Bottle 2	14	14	4.8	76	2.78
Bottle 3	14	14	5.1	75	1.4
Bottle 4	14	14	4.9	76	1.95

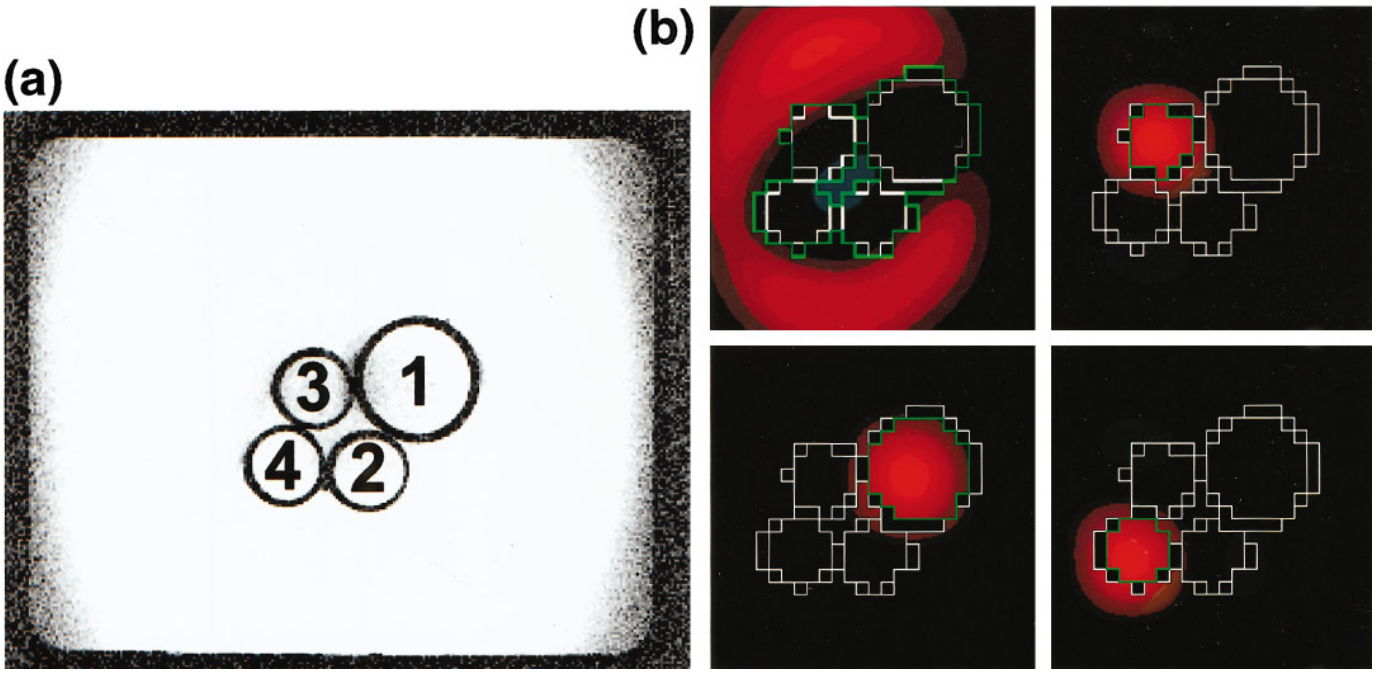

FIG. 3. (a) Proton image, showing the arrangement of the four phosphorus-containing bottles inside a larger flask. Each bottle corresponds to one compartment, indicated by the labels. Bottle 1 contains 48 ml of 0.75 M phosphate solution; bottles 2, 3, and 4 contain 14 ml each of 1.0, 0.5, and 0.75 M phosphate solution, respectively. The intensity variation is due to the inhomogeneous B_1 field of the surface coil, which would be even more pronounced in a vertical slice. (b) Spatial response function of the compartments in a coronal slice: Compartment of the container (upper left), compartment of bottle 3 (upper right), bottle 1 (lower left) and bottle 4 (lower right). The white lines delineate the compartments. The border of the respective target compartment is drawn in green. The color coding of the SRF is as follows: The magnitude of the SRF is encoded with brightness and the phase with color: Bright red regions contribute in phase to the compartmental signal, while regions with other bright colors add to the signal with the wrong phase; dark regions contribute little to the signal. It can be noticed that, in all cases, relevant contributions to the SRF mainly originate from within the compartmental volume.

average volume of the left ventricular wall was 175 ml ± 28 ml (mean ± st. dev.). The volume of the left ventricular blood was 58 ml ± 20 ml. These values are in good agreement with literature values of end-systolic volume (*40, 41*). There is a caveat in interpreting the result of any arbitrary compartment, since only volumes which are within the sensitive volume of the proton coil yield correct results.

Spectra of a volunteer obtained by SLOOP are given in Fig. 6. The spectra shown are the ones obtained from the left ventricular (LV) wall, the chest wall, and the blood pool of the

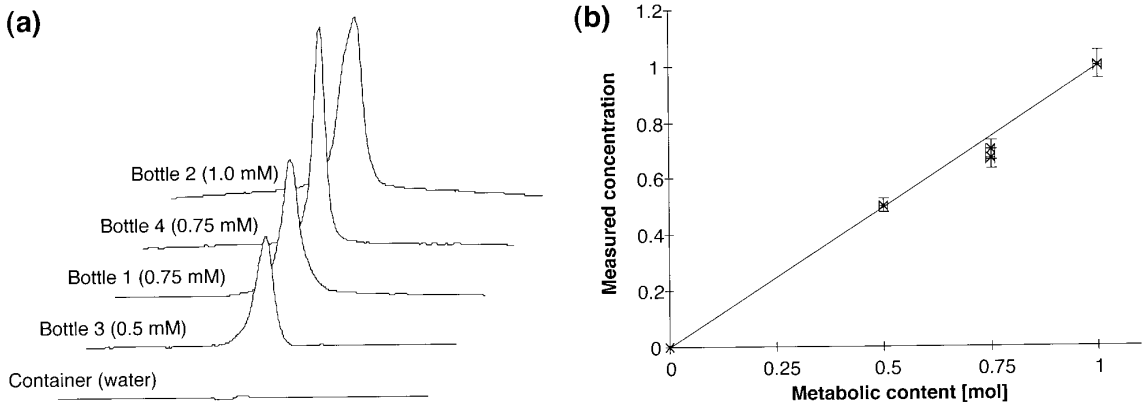

FIG. 4. (a) ^{31}P SLOOP spectra measured in the four bottles of the phantom shown in Fig. 3. Because of local differences in the shim, the shape and the width of these resonances vary. Good localization is demonstrated by complete absence of ^{31}P signal in the larger container. (b) Integrals of the resonances plotted versus known phosphate concentration. The crosses indicate the integrals; the slope of the regression line is 0.96. Quantification is possible with very good accuracy even though the B_1 field varies in a large amount over the volume of interest.

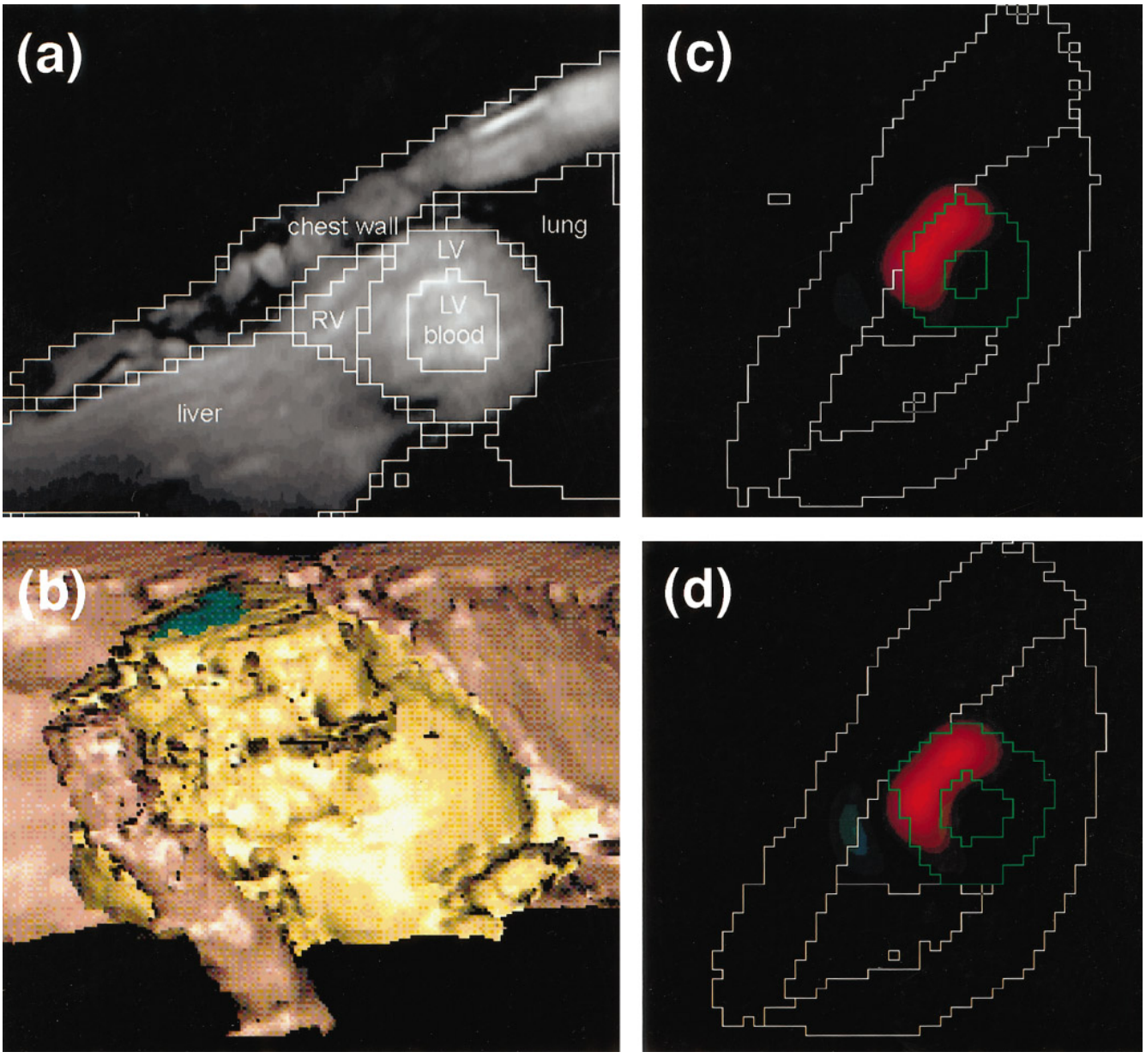

FIG. 5. (a) One out of 21 slices in the short axis ^{1}H images used for segmentation. Overlaid in white are the borders of the segmented compartments indicated by labels. The coarse resolution of these borders is due to a reduction of the matrix size after segmentation. This is irrelevant to the quality of the localization, because the spatial resolution of the spectroscopic experiment is inferior to that of ^{1}H imaging. This can be seen on images representing the spatial response functions. (b) 3D rendered image of segmented compartments: chest wall (red, back), LV wall (yellow), LV blood (green) and aorta (red, front). The whole stack of segmented slices was used for rendering. (c) and (d): two slices displaying the three-dimensional SRF of the LV compartment, showing the spatial origin of its spectrum. The color coding of the SRF is the same as in Fig. 3(b). The SRF and the resulting spectrum originate mostly from the anterior wall and the septum, because the SRF already embodies the sensitivity profile of the coil.

left ventricle. As expected, the PCr/ATP ratio is much higher in the chest wall than in the LV wall. A major contribution from 2,3-DPG is only seen in the spectrum from the LV blood, which indicates good localization.

The quantitative evaluation of the spectra from the LV wall of the volunteers was done with the T_1 values for PCr and ATP as stated earlier. This lead to a PCr/γ-ATP ratio of 1.90 $\pm$ 0.33 (mean $\pm$ st. dev., $n = 6$). This result agrees well with values of 1.83 $\pm$ 0.12 reported previously for saturation- and blood-corrected normal myocardium (average of several studies published, see Ref. *5*). A correction for varying NOE enhancement in different metabolites (*42*) was not applied to our data. In the chest wall a PCr/γ-ATP ratio of 4.11 $\pm$ 0.42 was obtained; here, also, no NOE correction was applied. The PCr/ATP ratio of the skeletal muscle is again in good agreement with values published previously (*43*, *44*). In the blood spectra, no quan-

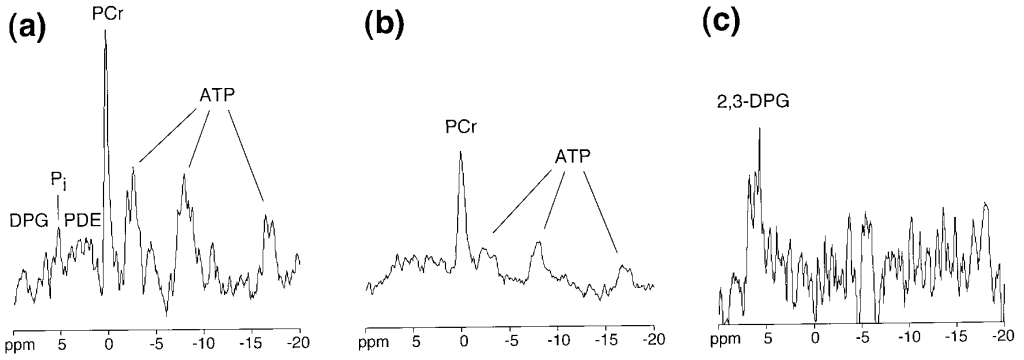

FIG. 6. SLOOP spectra from a volunteer. (a) Signal from the LV wall compartment; PCr and ATP are labeled. Resonances from 2,3-diphosphoglycerate (2,3-DPG), inorganic phosphate (P_i), and phosphodiester (PDE) are also identified. (b) Signal from the chest wall compartment. The increased SNR compared to the myocardial compartment is due to the fact that this compartment is larger and closer to the coil. In this compartment, the PCr/ATP is much higher compared to the spectrum in (a), since this spectrum contains mostly chest muscle. (c) Spectrum from the LV blood compartment. Because of the small size, the signal from this compartment is very noisy. Only signal from the 2,3-DPG from blood can be identified unambigiously. In all spectra, there appears a small artifact at −5 ppm. This is due to a glitch in the instrument; this artifact also showed up in the CSI spectra of this particular measurement. The spectra are scaled to a common maximum.

titative evaluation of relevant resonances was possible because of the low SNR of the spectra.

Detailed information about the spatial origin of the spectra can be gained by images of the SRF. Figures 5c and 5d depicts the SRF for the spectrum of the LV wall compartment in two slices of a volunteer. It can be seen that the SRF is localized well within the myocardium. Because of the B_1 profile of the coil, most of the signal originates from the anterior wall and the septum.

The SLOOP criteria in the left ventricular wall compartment did not vary much among the six volunteers, although the anatomical variations can be quite large. The localization criterion for the LV wall was $\mathscr{L} = 2.0 \pm 0.4$. The SLOOP efficiency was $\mathscr{E}_{\mathrm{SLOOP}} = 26.7\% \pm 1.4\%$. The quality of the localization can also be visualized *in vivo* with liver spectra, which have to be free of PCr. Figure 7 shows the spectrum of the left ventricular wall and the liver of another volunteer; no PCr is observable in the liver spectrum.

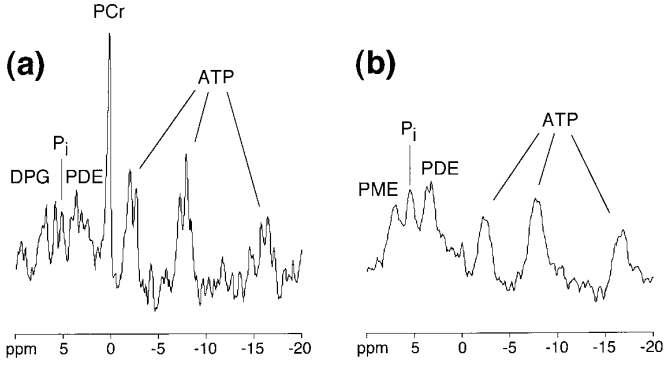

FIG. 7. (a) LV-wall spectrum of another volunteer. (b) Liver compartment: The absence of PCr demonstrates the high degree of localization. The small residual signal at the position of the PCr is dispersive, allowing the identification of this signal as contamination.

In Fig. 8 a CSI spectrum obtained from the LV as indicated on the small proton images is shown. This spectrum was calculated from the same raw data set as the spectra on Fig. 6. Comparison of the SNR in both data sets in the time domain results in an SNR advantage of $\sim 5.8/3.9 = 1.5$ for SLOOP over CSI. The SNR for CSI in a given data set was determined as the average of several reconstructions from the according "best" LV-CSI voxel. On average we found an SNR improvement of SLOOP over CSI of about 30%.

The improved SNR is a consequence of the larger volume of

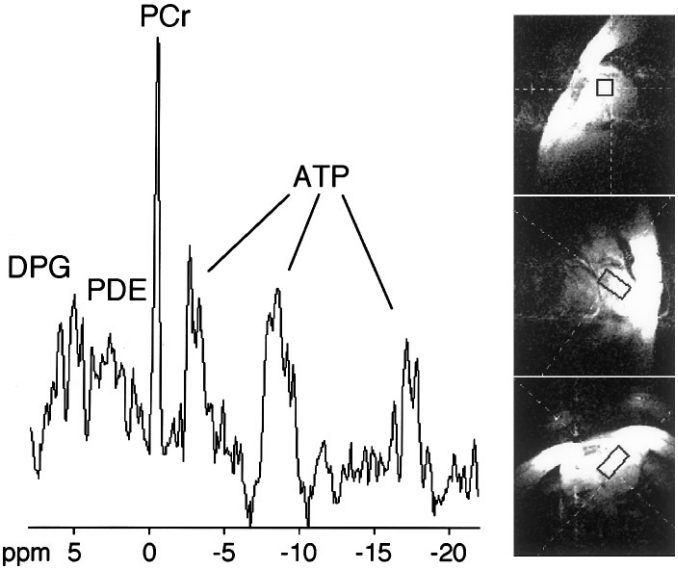

FIG. 8. Conventional CSI spectrum from the LV, reconstructed from the same data set as the data of Fig. 6. The spatial localization of the voxel can be determined on the scout images shown at right. This spectrum is very similar to the LV-wall SLOOP spectrum depicted in Fig. 6a. The SLOOP spectrum, however, has an advantage in the SNR of about 50%, due to better utilization of the target volume.

the left ventricular wall compartment of SLOOP compared to the according CSI voxel. Adding up several CSI voxels to get a comparable size in the resulting volume will not yield the same result, since the SNR does not scale linearly in this case (*39*) and the localization of the target volume decreases. The improved SNR is also confirmed by the efficiency $\mathscr{E}_{\mathrm{SLOOP}} = 27\%$ of the experiment. This shows that about a quarter of the total detectable magnetization (with the given experimental setup) from the left ventricular wall is detected by the SLOOP experiment.

DISCUSSION

The effort to implement a new method for cardiac NMR spectroscopy must be justified by improved localization properties or by better sensitivity (preferably by both). At the current state of the art, the poor SNR and the contamination arising from adjacent tissue are the major flaws of ^{31}P MRS in the human heart. SLOOP attempts to push this frontier further by exploiting all available *a priori* information, especially the knowledge of the size and the shape of the organ of interest. This knowledge is available through high-resolution NMR imaging in the same experimental setup. For some situations, a cautionary note is required: In brain, for instance, it is well known that the anatomical structures as seen in ^{1}H MRI do not necessarily reflect the distribution of the metabolites. NMR images of brain tumors are not a reliable source of *a priori* information which can be used in a SLOOP reconstruction. In the heart, however, the compartments of interest are well delineated on ^{1}H images, and these do provide the required knowledge about the geometry in the experimental setup.

The gain in sensitivity in a SLOOP experiment is mainly due to the larger voxel sizes: The shape of the sensitive region can be matched to the compartment of interest. This allows detection of the signals from a larger volume, without contamination from outside. Conventional techniques such as CSI or ISIS have to fit a more or less rectangular VOI into the myocardium, and therefore have to compromise the size of the VOI between sensitivity and contamination. A strict quantitative comparison between the sensitivities of CSI and SLOOP is difficult, because where SLOOP returns just one spectrum for "left ventricular myocardium," the SNR of the CSI spectrum depends to a large extent from the exact position of the VOI. Nevertheless, we did observe a slight gain in the SNR of most our SLOOP spectra in the six volunteers, which amounted on average to 30%. The absolute SNR of all our spectra is somewhat lower than what other authors have shown in the literature. This is due to the old design of the surface coil which we had to use in this study. Improved coil designs such as phased array coils (*45*) should provide a substantial improvement in sensitivity and should alleviate the problem of exact positioning of the coil on the subject.

The second issue is the quality of localization. Spectra from the heart suffer in particular from contamination with high signal levels from chest muscle, resulting often in erroneous PCr/ATP ratios. Again, SLOOP attempts to minimize the contamination by adjusting the sensitive region (which is best characterized by the spatial response function) to the compartment of interest. SLOOP also computes a quality criterion to evaluate the localization properties. This is a "worst case" criterion which evaluates the amplitude of the spatial response function outside the region of interest. In our experiments, we generally found a value of $\mathscr{L}$ of 2. For comparison, in an $8 \times 8 \times 8$ 3D-CSI experiment, the same criterion would yield $\mathscr{L} = 8.2$. This much higher value can not be compared directly to the value for SLOOP, because the profile of the B_1-field has not been taken into account, and because it has been obtained through integration over the whole FOV (instead of only over the volunteer). However, 3D CSI experiments are conducted every day and appear to provide reliable localization despite the high amplitude of the spatial response function outside the VOI. In one experimental setup, an abnormally high localization criterion has warned us that the surface coil was away from the isocenter of our instrument, and that there was a foldover of the spatial response function in a region of high sensitivity of the surface coil. This faulty situation would very likely have remained undetected without the computation of the quality criterion.

The actual contamination in a spectrum is very difficult to evaluate, and there is no theoretical criterion for it. The real contamination depends on all heterogeneities in the objects, including B_0 shifts and susceptibility variations. Contamination of course also arises from other sources—motion is a crucial issue. Phantom studies are not appropriate to fully evaluate the localization properties of a method, because phantoms normally are much less heterogeneous than a living subject. The heart spectra in our study show virtually no signals from blood, in any case much less than the CSI spectra processed from the same raw data. A second observation is that contamination in SLOOP spectra can often be recognized from an anomalous phase of the resonances. Contamination arises from regions where the phase cancellation in the SRF fails, and the SRF is likely to have a nonzero phase at that location. In the liver spectrum in Fig. 7, the residual resonance of PCr is dispersive, while all other resonances are in phase. Not being able to phase a SLOOP spectrum with the theoretically obtained values is a strong indication of spatial contamination. In our spectra, all SLOOP spectra from each experiment have received an identical zero- and first-order phase correction, and no major phase anomalies have been observed. This together with the observed spectral patterns makes us confident that the localization properties of SLOOP are appropriate.

SLOOP attempts to optimize the experimental parameters (FOV, flip angle, etc.) to yield the best possible experiment with the highest sensitivity and the best localization. Currently, no analytical solution is known which could provide rapidly a set of optimal parameters, and we had to employ the numerical optimization procedure described earlier. This algorithm is

computationally very demanding and takes far too long to be conducted while a subject lies waiting in the magnet. This, however, is not an issue, because for a given experimental setup (for instance, the human heart) the optimal parameters are very similar. For each typical situation, the experimental parameters therefore can be optimized once for all, and these parameters can be used for that protocol. In our human studies, we have only used a regular gridding of *k*-space until now. It is known from other studies (*46–48*) and also from our original work on SLOOP (*21*) that radial, hexagonal or weighted sampling schemes of *k*-space provide superior localization. Such schemes unfortunately are rather difficult to implement on a clinical NMR instrument.

To detect viable myocardium, it might be crucial that the absolute concentration of metabolites can be measured (*4*). SLOOP is in principle a very convenient method to achieve absolute quantification. It intrinsically takes into account the volume of the compartments, the variation of the excitation angles and the associated variation of the spin saturation, the spatially varying sensitivity of a surface coil, and all other parameters which are known about the instrument, the experiment, and the sample. Our phantom study has demonstrated that indeed the concentration in the different compartments can be accurately measured. Local spin saturation is an integral part of the model, and no saturation correction needs to be applied when evaluating the local spectra. On the other hand, this requires that all processing steps be repeated for each individual resonance, which is not a big issue with the computing power available today. Nevertheless, a few obstacles remain to be solved before absolute concentration can be measured reliably in the human heart. A major issue is nuclear Overhauser enhancement. The exact value of NOE in various tissue is not accurately known, and it is unclear whether it changes with pathology. NOE is also dependent on the B_1 homogeneity of the ^{1}H coil, and this is not included in our model. Other issues are the relaxation times, the accuracy of the segmentation, and—last but not least—the procedure to measure the amplitudes in local spectra. Many more experiments need to be done to address these issues.

CONCLUSION

We presented a method for clinical cardiac ^{31}P spectroscopy which is easy to use and yields more accurate information than conventional methods. The only major additional effort compared to CSI is the segmentation of the proton images. Current segmentation algorithms do not allow for fully automated segmentation of data with a low contrast-to-noise ratio acquired in inhomogeneous B_1 fields. Therefore, at the current time, segmentation has to be done manually. The results of the volunteer measurements are in accordance with published literature. We were able to prove the reliability and accuracy of the method in addition by phantom measurements, which showed a high correlation between expected and measured results. The reliability of a single experiment can be assessed by the SLOOP parameters obtained mathematically.

We showed the feasibility of SLOOP in cardiac spectroscopy. The next step to take is to prove clinical relevance in a study which includes a population of patients with cardiac diseases. Additions to the experimental setup could permit immediate absolute quantification of spectral data. The direct assessment of metabolite concentrations would allow the quantification of myocardial energy metabolism. The knowledge of absolute metabolic concentrations may provide new insights into cardiac disease, such as ischemia and dilated cardiomyopathy.

ACKNOWLEDGMENTS

We are indebted to Peter Bachert from the "Deutsches Krebsforschungszentrum," Heidelberg, for making measurement time available. The authors gratefully acknowledge financial support by Siemens Medizintechnik (RL), "Deutsche Forschungsgemeinschaft" (MvK: Ki 433/2-1, Ki 433/2-2), and the BMBF project "Medizin 2000—Interdisziplinäres Zentrum für medizinische Forschung (Projekt F2)."

REFERENCES

1. P. A. Bottomley, Noninvasive study of high-energy phosphate metabolism in human heart by depth-resolved ^{31}P NMR spectroscopy, *Science* **229,** 769–772 (1985).
2. R. G. Weiss, P. A. Bottomley, C. J. Hardy, and G. Gerstenblith, Regional myocardial metabolism of high-energy phosphates during isometric exercise in patients with coronary artery disease, *N. Engl. J. Med.* **323,** 1593–1600 (1990).
3. S. Neubauer, T. Krahe, R. Schindler, M. Horn, H. Hillenbrand, C. Entzeroth, H. Mader, E. P. Kromer, G. A. J. Reiger, K. Lackner, and G. Ertl, ^{31}P magnetic resonance spectroscopy in dilated cardiomyopathy and coronary artery disease, *Circulation* **86,** 1810–1818 (1992).
4. T. Yabe, K. Mitsunami, T. Inubushi, and M. Kinoshita, Quantitative measurements of cardiac phosphorus metabolites in coronary artery disease by ^{31}P magnetic resonance spectroscopy, *Circulation* **92,** 15–23 (1995).
5. P. A. Bottomley, MR spectroscopy of the human heart: The status and the challenges, *Radiology* **191,** 593–612 (1994).
6. G. M. Pohost, Is ^{31}P-NMR spectroscopic imaging a viable approach to assess myocardial viability?, *Circulation* **92,** 9–10 (1995).
7. H. P. Beyerbacht, H. W. Vliegen, H. J. Lamb, J. Doornbos, A. de Roos, A. van der Laarse, and E. E. van der Wall, Phosphorus magnetic resonance spectroscopy of the human heart: Current status and clinical implications, *Europ. Heart J.* **17,** 1158–1166 (1996).
8. M. J. Blackledge, B. Rajagopalan, R. D. Oberhaensli, N. M. Bolas, P. Styles, and G. K. Radda, Quantitative studies of human cardiac metabolism by ^{31}P rotating frame NMR, *Proc. Natl. Acad. Sci.* **84,** 4283–4287 (1987).
9. R. J. Ordidge, A. Connelly, and J. A. B. Lohman, Image-selected *in vivo* spectroscopy (ISIS). A new technique for spatially selective NMR spectroscopy, *J. Magn. Reson.* **66,** 283–294 (1986).
10. T. R. Brown, B. M. Kincaid, and K. Uğurbil, NMR chemical shift imaging in three dimensions, *Proc. Natl. Acad. Sci. USA* **79,** 3523–3526 (1982).
11. R. S. Menon, K. Hendrich, X. Hu, and K. Uğurbil, ^{31}P NMR spectroscopy of the human heart at 4 T: Detection of substantially

uncontaminated cardiac spectra and differentiation of subepicardium and subendocardium, *Magn. Reson. Med.* **26,** 368–376 (1992).

12. A. deRoos, J. Doornbos, P. R. Luyten, L. J. M. P. Oosterwaal, E. E. van der Wall, and J. A. den Hollander, Cardiac metabolism in patients with dilated and hypertrophic cardiomyopathy: Assessment with proton-decoupled P-31 MR spectroscopy, *J. Magn. Reson. Imag.* **2,** 711–719 (1992).
13. D. B. Twieg, D. J. Meyerhoff, B. Hubesch, K. Roth, D. Sappey-Marinier, M. D. Boska, J. R. Gober, S. Schaefer, and M. W. Weiner, Phosphorus-31 magnetic resonance spectroscopy in humans by spectroscopic imaging: Localized spectroscopy and metabolite imaging, *Magn. Reson. Med.* **12,** 291–305 (1989).
14. S. Schaefer, J. R. Gober, G. G. Schwartz, D. B. Twieg, M. W. Weiner, and B. Massie, *In vivo* phosphorus-31 spectroscopic imaging in patients with global myocardial disease, *Am. J. Cardiol.* **65,** 1154–1161 (1990).
15. H. Kolem, R. Sauter, M. Friedrich, M. Schneider, and K. Wicklow, "Cardiovascular Applications of Magnetic Resonance," Chap. 33, pp. 417–426, Futura Publishing Company, New York (1993).
16. H. P. Hetherington, D. J. E. Luney, J. T. Vaughan, J. W. Pan, S. L. Ponder, O. Tschendel, D. B. Twieg, and G. M. Pohost, 3D-^{31}P spectroscopic imaging of the human heart at 4.1 T, *Magn. Reson. Med.* **33,** 427–431 (1995).
17. P. A. Bottomley, C. J. Hardy, and P. B. Roemer, Phosphate metabolite imaging and concentration measurements in human heart by nuclear magnetic resonance, *Magn. Reson. Med.* **14,** 425–434 (1990).
18. A. A. Maudsley, Sensitivity in Fourier imaging, *J. Magn. Reson.* **68,** 363–366 (1986).
19. M. Decorps and D. Bourgeois, "Localized Spectroscopy Using Static Magnetic Field Gradients: Comparison of Techniques," Chap. 5, pp. 119–149, Number 27 in NMR Basic Principles and Progress, Springer, Berlin (1992).
20. P. A. Bottomley, E. Atalar, and R. G. Weiss, Human cardiac high-energy phosphate metabolite concentrations by 1D-resolved NMR spectroscopy, *Magn. Reson. Med.* **35,** 664–670 (1996).
21. M. von Kienlin and R. Mejia, Spectral localization with optimal pointspread function, *J. Magn. Reson.* **94,** 268–287 (1991).
22. D. I. Hoult and R. E. Richards, The signal-to-noise ratio of the nuclear magnetic resonance experiment, *J. Magn. Reson.* **24,** 71–85 (1976).
23. R. R. Ernst and W. A. Anderson, Application of Fourier transform spectroscopy to magnetic resonance, *Rev. Sci. Instr.* **37,** 93–102 (1966).
24. X. Hu, D. N. Levin, P. C. Lauterbur, and T. Spraggins, SLIM: Spectral localization by imaging, *Magn. Reson. Med.* **8,** 314–322 (1988).
25. F. J. Harris, On the use of windows for harmonic analysis with the discrete Fourier transform, *Proc. IEEE* **66,** 51–83 (1978).
26. K. F. King and P. R. Moran, A unified description of NMR imaging, data-collection strategies, and reconstruction, *Med. Phys.* **11,** 1–14 (1984).
27. H. R. Brooker, T. H. Mareci, and J. Mao, Selective Fourier transform localization, *Magn. Reson. Med.* **5,** 417–433 (1987).
28. T. H. Mareci and H. R. Brooker, High-resolution magnetic resonance spectra from a sensitive region defined with pulsed field gradients, *J. Magn. Reson.* **57,** 157–163 (1984).
29. D. L. Parker, G. T. Gullberg, and P. R. Frederick, Gibbs artifact removal in magnetic resonance imaging, *Med. Phys.* **14,** 640–645 (1987).
30. Z.-P. Liang, H. Lee, and P. C. Lauterbur, On errors of the SLIM technique, *in* "Proceedings of the Society of Magnetic Resonance in Medicine," p. 1077, Society of Magnetic Resonance in Medicine (1990).
31. W. M. M. J. Bovee, A. F. Keevil, M. O. Leach, and F. Podo, Quality assessment in *in vivo* spectroscopy: II. A protocol for quality assessment, *MRI* **13,** 123–129 (1995).
32. S. K. Plevritis, Resolution improvements for magnetic resonance spectroscopic images, Ph.D. Thesis, Stanford University (1992).
33. K. Wicklow, Methoden und Anwendungen von ^{31}P-^{1}H Doppelresonanztechniken für die *in vivo* NMR-Spektroskopie, Ph.D. Thesis, Johann Wolfgang Goethe–Universität Frankfurt am Main (Germany) (1994).
34. S. Röll, Segmentieren und Visualisieren dreidimensionaler MR-Bilder am Beispiel eines perfundierten Herzens, Master's Thesis, Universität Würzburg, Germany (1993).
35. P. Henz, Dreidimensionale Bildverarbeitung von NMR-Datensätzen, Master's Thesis, Universität Würzburg, Germany (1994).
36. R. Löffler, H. Kolem, K. Wicklow, A. Haase, and M. von Kienlin, Localized MR spectra in the human heart from anatomically matched compartments in three spatial dimensions, *in* "Proceedings of the Society of Magnetic Resonance," p. 334, Society of Magnetic Resonance (1995).
37. J. Kreß, Quantitative Segmentation mehrdimensionaler NMR-Bilddaten, Master's Thesis, Universität Würzburg, Germany (1996).
38. P. A. Bottomley and R. Ouwerkerk, Optimum flip-angles for exciting NMR with uncertain T1 values, *Magn. Reson. Med.* **32,** 137–141 (1994).
39. M. von Kienlin, Empfindlichkeit und Ortsauflösung in der lokalisierten NMR-Spektroskopie, Habilitation Thesis, Universität Würzburg, Germany (1996).
40. J. Wynne, L. H. Green, T. Mann, D. Levin, and W. Grossman, Estimation of left ventricular volumes in man from biplane cineangiograms filmed in oblique projections, *Am. J. Cardiol.* **41,** 726–732 (1978).
41. J. W. Kennedy, J. G. Doces, and D. K. Stewart, Left ventricular function before and following surgical treatment of mitral valve disease, *Amer. Heart J.* **97,** 592–598 (1979).
42. P. A. Bottomley and C. J. Hardy, Proton Overhauser enhancement in human cardiac phosphorus NMR spectroscopy at 1.5-T, *Magn. Reson. Med.* **24,** 384–390 (1992).
43. J. A. Bittl, J. DeLayre, and J. S. Ingwall, Rate equation for creatine kinase predicts the *in vivo* reaction velocity: ^{31}P NMR surface coil studies in brain, heart, and skeletal muscle of the living rat, *Biochemistry* **26,** 6083–6090 (1987).
44. K. M. Brindle, M. J. Blackledge, R. A. J. Challiss, and G. K. Radda, ^{31}P NMR magnetization-transfer measurements of ATP turnover during steady-state isometric muscle contraction in the rat hind limb *in vivo, Biochemistry* **28,** 4887–4893 (1989).
45. C. J. Hardy, P. A. Bottomley, K. W. Rohling, and P. B. Roemer, An NMR phased array for human cardiac ^{31}P spectroscopy, *Magn. Reson. Med.* **28,** 54–64 (1992).
46. T. H. Mareci and H. R. Brooker, Essential considerations for spectral localization using indirect gradient encoding of spatial information, *J. Magn. Reson.* **92,** 229–246 (1991).
47. A. A. Maudsley, G. B. Matson, J. W. Hugg, and M. W. Weiner, Reduced phase encoding in spectroscopic imaging, *Magn. Reson. Med.* **31,** 645–651 (1994).
48. Y. L. Fur and M. von Kienlin, Acquisition weighted chemical shift imaging of the isolated rat heart at 11.7 Tesla, *in* "Proceedings of the Society of Magnetic Resonance," p. 1915, Society of Magnetic Resonance (1995).